Journal of
Applied Remote Sensing

RemoteSensing.SPIEDigitalLibrary.org

APIS: the miniaturized Earth observation camera on-board OPTOS CubeSat

Daniel Garranzo
Armonía Núñez
Hugo Laguna
Tomás Belenguer
Eduardo de Miguel
María Cebollero
Sergio Ibarmia
César Martínez

SPIE.

Daniel Garranzo, Armonía Núñez, Hugo Laguna, Tomás Belenguer, Eduardo de Miguel, María Cebollero, Sergio Ibarmia, César Martínez, “APIS: the miniaturized Earth observation camera on-board OPTOS CubeSat,” *J. Appl. Remote Sens.* **13**(3), 032502 (2019), doi: 10.1117/1.JRS.13.032502.

APIS: the miniaturized Earth observation camera on-board OPTOS CubeSat

Daniel Garranzo,[a,*] Armonía Núñez,[a] Hugo Laguna,[a] Tomás Belenguer,[a]
Eduardo de Miguel,[a] María Cebollero,[b] Sergio Ibarmia,[a]
and César Martínez[a]
[a]Instituto Nacional de Técnica Aeroespacial, Torrejón de Ardoz, Spain
[b]Ingeniería de Sistemas para la Defensa de España, S.A (ISDEFE), Madrid, Spain

Abstract. The athermalized panchromatic imaging system (APIS) was the low-resolution refractive camera proposed by the Laboratorio de Instrumentación Espacial as a CubeSat payload. APIS flew on-board OPTOS CubeSat designed and developed by INTA using the methodology of European Cooperation for Space Standardization and space qualification tests. APIS had two main objectives: to analyze the performance degradation of commercial off-the-shelf (COTS) components due to space radiation and to verify in-flight functionality of the passive athermalization system. We summarize the design, manufacturing, and assembly integration and verification phases of the instrument, as well as the analysis of the radiation tests. Additional studies are included, such as thermal behavior, tolerances and sensitivity analysis, signal-to-noise ratio, and ghost images, as well as their implications during the design process. Three main goals were achieved during the mission lifetime: (1) the viability of a small refractive Earth observation camera on-board a CubeSat, (2) the validation for low Earth orbits of a passive athermalization system, and (3) the use of COTS elements, such as commercial glasses and detectors based on complementary metal–oxide–semiconductor technology, on a 2-year Earth observation mission. [DOI: 10.1117/1.JRS.13.032502]

Keywords: camera; athermalization; CubeSat; Earth observation; radiation; commercial off-the-shelf.

Paper 180861SS received Oct. 26, 2018; accepted for publication Feb. 21, 2019; published online May 10, 2019.

1 Introduction

The CubeSat standard was developed in 1999.[1] This development opened a low-cost opportunity to design, manufacture, and test small satellites for low Earth orbits (LEO). Therefore, CubeSats allow testing new spacecraft technologies, scientific experiments, miniaturized optical instruments, etc., whose cost would not be justifiable in a larger satellite. Following this idea, the OPTOS nanosatellite was intended to qualify the platform and payloads in orbit.

The OPTOS CubeSat was launched on November 21, 2013 from the Yasny Cosmodrome (Russia) as a secondary payload on a Dnepr-1 launch vehicle. International Space Company Kosmotras operated the launch.

OPTOS included four payloads: (1) athermalized panchromatic imager system (APIS), (2) fiber Bragg gratings for optical sensing (FIBOS) to measure temperature, (3) giant magnetoresistance system (GMR) to measure the magnetic fluxes produced by Earth's magnetic field, and (4) OPTOS dose monitoring (ODM) to measure the radiation environment in space. However, 10 technologies were tested for their qualification in space. For example, a distributed on-board data handling subsystem based on field programmable gate arrays and complex programmable logic devices, an optical wireless communication system (OBCom) with the implementation of a reduced controller area network (CAN) protocol and an internal structure based on composite materials,[2–9] among others.

---

*Address all correspondence to Daniel Garranzo, E-mail: garranzogid@inta.es

The nanosatellite external structure corresponded to the triple CubeSat format (3U) in size and mass, i.e., 10 cm × 10 cm × 34.5 cm, and ∼3.8 kg. Internally, a composite structure was selected to support all the elements and to allow easy integration and tests. The spacecraft structure featured an external aluminum casing provided by Pumpkin Inc. of San Francisco, California, and an internal carbon fiber structure, designed and manufactured by INTA.[10–12]

OPTOS CubeSat was a technological challenge regarding the size and cost reduction. These constraints forced certain design decisions. For example, the development of a deployment system for the solar panels to double the nanosatellite power as it is shown in Fig. 1(a), and wireless communications, the positioning of the payloads and subsystems into the internal structure in a rack way, and a miniaturized Earth observation camera shown in Fig. 1(b).

The APIS camera had two objectives during the mission lifetime. The first one was to evaluate the space radiation damage on commercial off-the-shelf (COTS) components and the second one to verify the functionality of the passive athermalization mechanical system. Both objectives would be evaluated through image analysis.

The restrictive requirements on size and weight resulted in a compact device with APIS external envelope dimensions of 57 mm × 46 mm × 35.7 mm and 120 g weight (see Fig. 2). On the other hand, the low power consumption requirement was met using complementary metal–oxide–semiconductor technology in the focal plane.

APIS performed Earth observations in the visible spectrum from an elliptical orbit of 600 × 800 km with an inclination of 97.8 deg. The expected mission lifetime was established in one year.

The nanosatellite incorporated a pyrotechnic shutter (as shown in Fig. 3) in order to avoid direct Sun light into the camera during the launch and commissioning phases.

2 Instrument Concept

This section describes the three main parts that make up the APIS camera concept: the optical system, the electronics design, and the mechanical design.

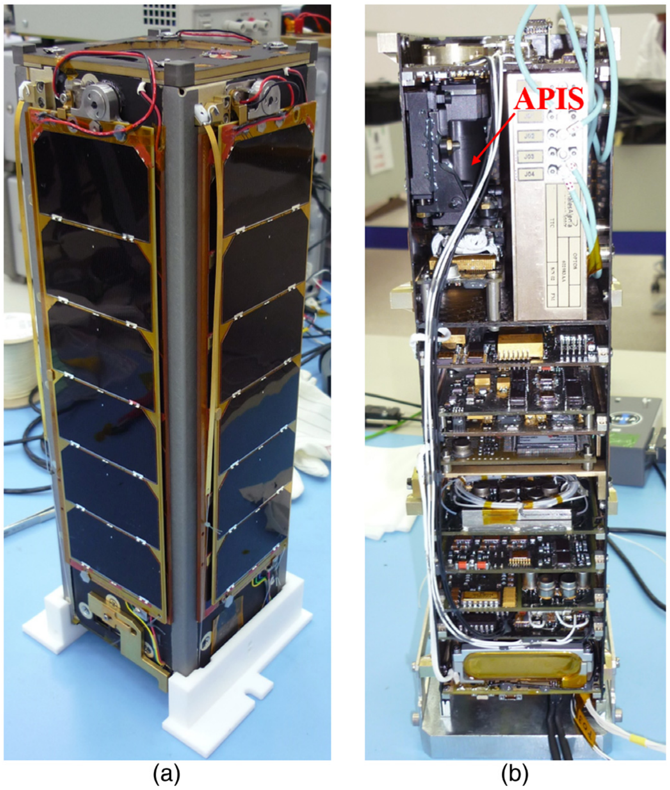

Fig. 1 (a) OPTOS satellite in launch configuration with the panels folded and (b) OPTOS internal structure with APIS assembled in the upper left part.

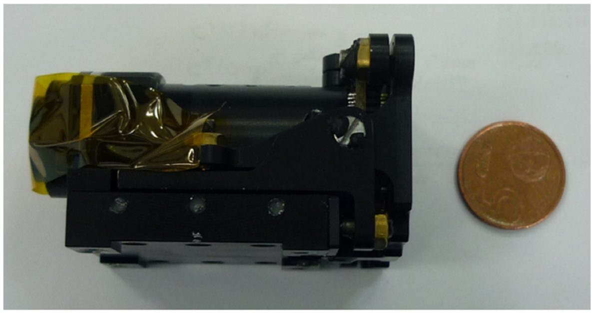

Fig. 2 APIS camera compared to a 5 euro cent coin.

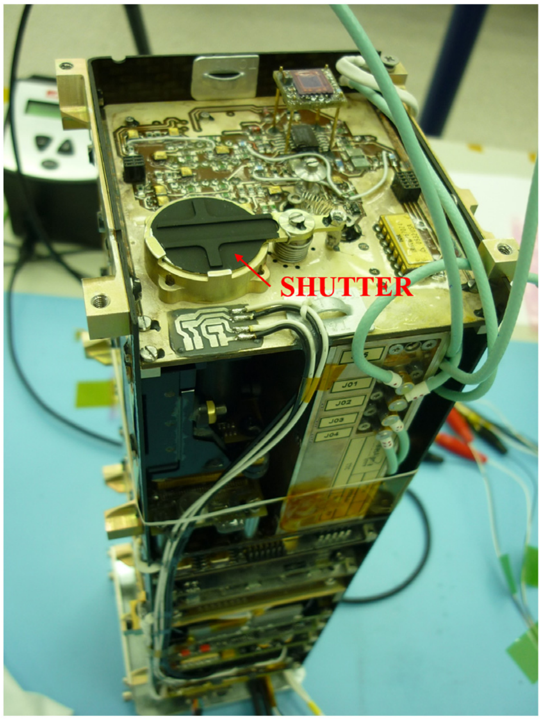

Fig. 3 Shutter closed in the upper part of the OPTOS internal structure.

2.1 *APIS Optical System*

The optical system was a refractive objective working in the visible spectral band (450 to 650 nm). It was designed using the optical design software CODE V from Synopsis® Inc. The objective consisted of a triplet with a conic surface and two meniscus lenses close to the focal plane (see Fig. 4). This configuration reduced residual aberrations in the image, such as astigmatism, spherical, and field curvature.

The system was designed with an external aperture stop and three different glasses from the Schott catalog: NFK51, NSF57, and NLASF41.

Figure 4 shows the optical layout which includes the protective window of the selected detector for APIS camera (the IBIS5-B-1300[13] CMOS image sensor).

The optical system with a 2.5 f-number (20-mm focal length and 8-mm pupil diameter) was optimized, using the modulation transfer function (MTF) as merit function, for an asymmetric field of view (FOV) of 12.16 deg × 9.25 deg and a pixel size of 6.7 μm. This FOV was equivalent to a rectangular Earth swath between 128 km × 97 km and 170 km × 129 km. It also provided a resolution between 201 and 268 m, depending on the orbit height.

Some additional studies, such as thermal behavior, tolerances, and sensitivity analysis, signal-to-noise ratio (SNR) and ghost images, were performed during the critical design phase

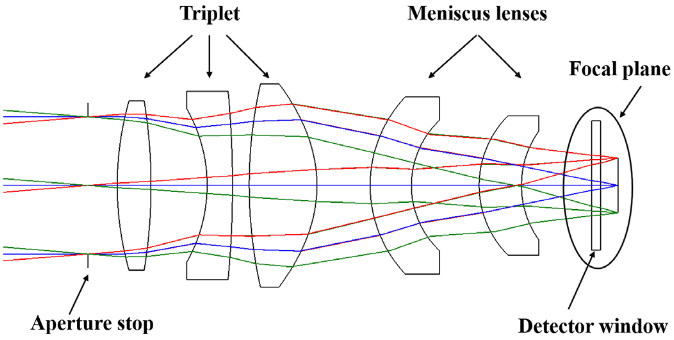

Fig. 4 APIS camera optical layout.

because of their implications in the mechanical design and manufacturing phases. The main conclusions obtained from these studies are detailed from Secs. 2.1.1 to 2.1.4.

2.1.1 *Thermal-vacuum behavior*

APIS would be subject to vacuum conditions and temperature changes during flight operation with the consequent performance degradation due to the environment. The APIS behavior due to these environmental changes had to be analyzed in order to guarantee its optical performance in flight.

The thermal-vacuum behavior was simulated with CODE V for APIS operational conditions: vacuum and a ±20°C temperature range. For these conditions, the image degradation was separately evaluated as nominal focus shifts (-26.5 μm due to vacuum and ± 18 μm due to temperature range). The result of the analysis was focus shifts greater than the APIS focus depth (± 7 μm in average for the spectral band). As a consequence, it was proposed that the focus shift due to vacuum conditions be compensated at the laboratory before APIS launch. However, the thermal focus shift expected during the APIS flight operation indicated that an athermalization mechanical system was required.

2.1.2 *Tolerances and sensitivity analysis*

The objective of this analysis (performed with CODE V) was to define a manufacturing and assembly tolerances budget. It also determined the best set of compensators that could simulate the assembly and necessary alignment process to recover the image quality of the instrument.

The APIS tolerances budget was highly critical (taking into account the reduced dimensions of the system) as the second and third lenses are the most critical elements. Therefore, the focal plane was chosen as the best tolerances compensator. In particular, linear displacement along the optical axis and tilts of the APIS focal plane should be able to be adjusted during the APIS alignment phase. These requirements about the assembly and alignment process were considered in the mechanical design.

2.1.3 *Signal-to-noise ratio study*

This study was performed to evaluate the performance of the electro-optical instrument. In particular, in the case of an instrument for Earth observation, the signal comes from the scene that is considered as an extensive source of certain radiance. Therefore, three kinds of scenes (assuming different latitudes and illumination conditions) were taken into account for the APIS signal evaluation: desert/snow/ice areas (high reflectance), oceanic areas (low reflectance), and land areas. Regarding the noise evaluation, only four sources of noise were considered: photonic noise, readout noise, digital noise, and dark noise. The criterion followed in the analysis was to obtain an SNR value better than 100:1 for average illumination conditions (typical value for an electro-optical system).

The irradiance on the detector depends on the scene radiance, the optical transmission, and the f-number of the instrument. The low f-number of APIS already indicated that a high irradiance on the detector would be expected. In addition, the integration time regulates the energy received in each pixel.

The frame period of the IBIS5-B-1300 sensor depends on the shutter type (see Ref. 13). In the snapshot shutter mode (selected for APIS camera), the minimum read out time of the full resolution at nominal speed (40 MHz pixel rate) is obtained with an integration time of 1 ms. This minimum value of the integration time produced saturation of the detector for the scenes with high reflectance (desert/snow/ice areas).

Therefore, the main result of this SNR evaluation was that a neutral-density filter (with $T \leq 15\%$) should be used at the entrance of the instrument to avoid saturation of the detector.

In this way, an SNR value better than 100:1 and an optimal detector response (dynamic range) could be obtained by considering a different integration time for each scene.

The selected filter was the NG5 from the Schott catalogue with 3.3 mm thickness. This neutral-density filter was used as substrate of the bandpass filter required for the APIS camera that was specified and designed by the Laboratorio de Instrumentación Espacial (LINES) at INTA. The design consisted of a combination of multilayer edges filters on both filter surfaces. The transmittance of the final bandpass/neutral-density filter fulfilled the requirement obtained from the SNR study.

2.1.4 *Ghost images*

This study was performed with the Advanced Systems Analysis Program (ASAP) from Breault Research Organization Inc. The objective of the study was to analyze the influence in the APIS point spread function (PSF) produced by retroreflections on the optical surfaces. The study consisted of finding the most relevant energetic paths and analyzing the relation between the energy collected by the ghost images and the PSF of the system.

The main contributions to the generation of ghost images were related to the interaction of the CMOS reflections and the flat surfaces (filter and detector window), and retroreflections of the meniscus lenses. The study verified that using high antireflection coatings in the optical components ($T > 99\%$) resulted in a flux ratio of the ghost images/signal of 10^{-3}.

Figure 5 shows the global PSF flux in the focal plane (with the ghost process included) for a 100-W energy incident. Figure 6 shows the corresponding flux of the ghost image process separately.

Therefore, the influence of the ghost images was negligible. Ghost images were on the same order as the inherent noise of the system.

2.2 *APIS Electronic Design*

The selected detector for the APIS camera was the IBIS5-B-1300 model from Cypress Inc. (currently ON Semiconductor®) in a monochrome version. The IBIS5-B-1300 is a CMOS image

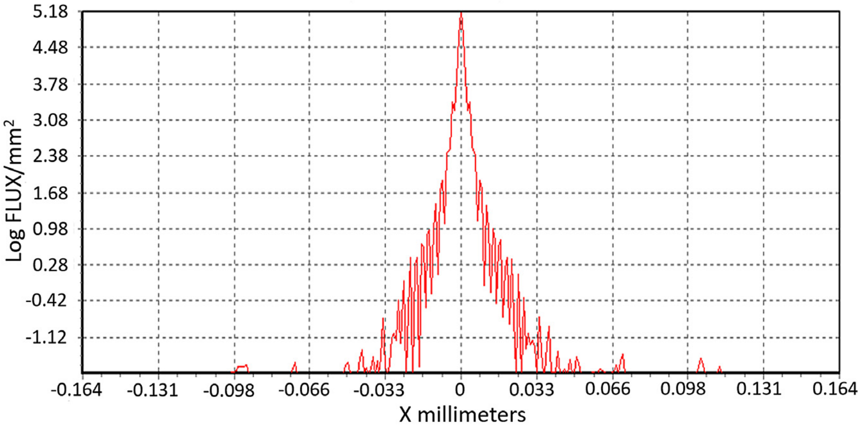

Fig. 5 Global PSF including the ghost image process (0.657046 W total flux).

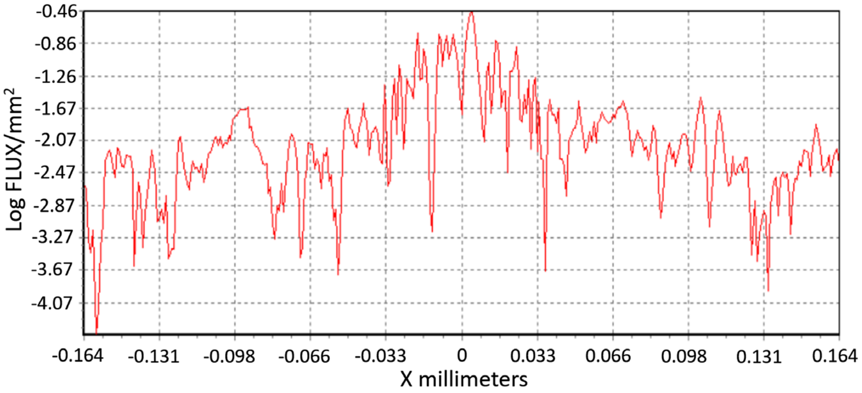

Fig. 6 Ghost image process (0.000476 W total flux).

sensor that integrates several functionalities. It performs as an analog-image acquisition system, a digitizer, and a digital signal processing system. The main key performance parameters of the sensor can be seen in Ref. 13.

The APIS camera was optimized for a focal plane size of 4.3 mm × 3.2 mm corresponding to a region of interest (ROI) of 640 × 480 pixels in order to boost the readout speed. The sensor worked in snapshot shutter mode.

The electronic design of APIS was divided in two boards as shown in Fig. 7: the APIS focal plane board, which includes the CMOS image sensor and a temperature sensor, and the APIS main board with the rest of the electronic devices.

The APIS focal plane board was connected to the APIS main board by a flexible cable with 10 data lines, 14 control lines, and 2 power lines.

2.3 *APIS Optomechanical Design*

The APIS optomechanical design had five important design challenges. (1) Geometrical: the APIS camera had to be installed inside a cubic prism volume of 65 mm × 52 mm × 36.4 mm. (2) Weigh: the APIS camera had to weigh less than 150 g. (3) Tolerances: critical position tolerances of the optical elements had to be maintained. (4) Thermal: the mechanical design had to

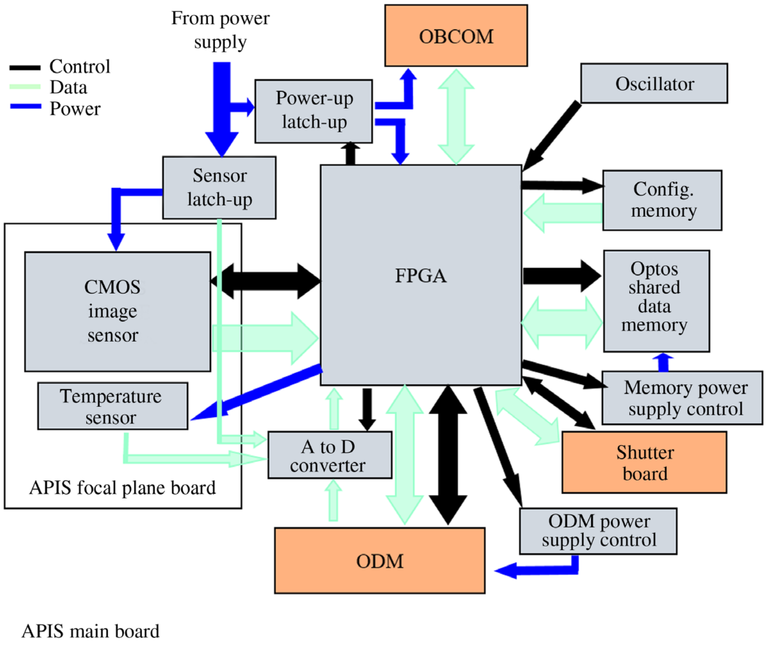

Fig. 7 APIS electronics diagram.

absorb the optical distance changes induced by the thermal expansion (passive athermalization system). (5) Stray-light protection: the APIS camera had to avoid the stray-light radiation by means of baffles at the entrance of the instrument and in the detector area.

2.3.1 *Mechanical subassemblies*

The most important subassemblies of the APIS optomechanical design can be identified in Fig. 8 by different colors. The platform subassembly is formed by the base part (dark red part) that allows the system to be attached to the lateral wall of OPTOS CubeSat, the sliding part (green part), and two linear sliding elements to join them. Also shown is the optical subassembly, which includes the five mounted lenses, the tube to hold them (dark blue part) and the support for all of it (yellow part) with the venting slots. Next is the focal plane subassembly, which is formed by the electronic card with the detector itself. This subassembly provides the system with the ability to tilt the focal plane array with respect to orthogonal axes by means of a gimbaled platform. Finally, the baffle subassembly formed by the baffle itself (including the aperture stop) and the bandpass/neutral density filter that was glued on it.

2.3.2 *Focal plane movements and adjustments*

In order to comply with the critical alignment requirements of the focal plane (movement ranges/accuracies) during the assembly integration and verification (AIV) phase, the optomechanical design provided the system with the ability to change optical-axis distance and two tilting angles of the focal plane. The linear movement along the optical-axis was achieved by the relative displacement between the two main parts of the platform subassembly. The use of linear guideways (R1-030 model), 30 mm long from Schneeberger GmbH and an ultrafine adjustment couple thread/screw (F3SS8 model with 250 $\mu\text{m/rev}$) from Thorlabs Inc. allowed a micrometric displacement. Moreover, a tilting movement was achieved by using two small bearings and the aforementioned ultrafine adjustment couple thread/screw for each rotation axis.

We have also used these linear guideways in the full disk telescope refocusing mechanism[14] for the Solar Orbiter ESA Mission, successfully developed at our laboratory.

2.3.3 *Lens mounting*

The critical positioning tolerances together with the small diameter of the lenses (10 mm in average) led to identifying the lens mounting as one of the most critical problems of this design. The best solution was to glue every lens to an individual mount (AL-6082-T6 material) with RTV560 red silicone. The gluing process was carried out on a centering machine to check the centering and tilting of each lens during the glue curing time. All the mounts had the same diameter for an easier assembly into the lens tube (dark blue part in Fig. 8).

Moreover, eight positioning notches were performed in the mount of the most critical lens (conic lens) in order to be able to rotate the lens through the venting slots during the alignment phase.

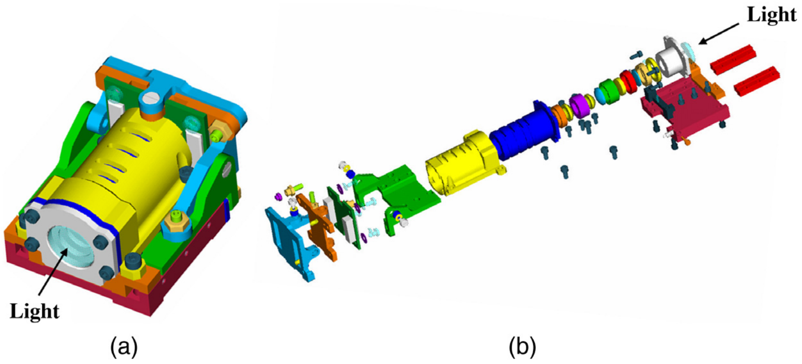

Fig. 8 APIS optomechanical design: (a) CAD view and (b) exploded view.

2.3.4 *Athermalization system*

The passive athermalization system was accomplished by selecting different materials for the parts that held the lenses pack. In particular, the tube in which all the five lenses were mounted in cascade was made of INVAR (dark blue part in Fig. 8) which has a practically zero coefficient of thermal expansion. In addition, this lens barrel was mounted into an aluminum part (yellow part in Fig. 8). This placement produced a distance variation between the apex of the fifth lens and the focal plane that remained within the focus depth of the system for a temperature range of 40 K. That means that the proposed mechanical design was able to absorb the optical focus shift (see Sec. 2.1.1) due to the changes in the optical properties of the elements affected by temperature.

The experimental verification of this can be seen in Sec. 4.5 (Table 6). The maximum change in the APIS focus produced during a 40 K thermal excursion (in vacuum conditions) was 4.9 μm (below the focus depth).

2.3.5 *Baffles*

In order to reject unwanted light into the FOV, the entrance baffle was a piece with an internal cone 15 deg wide configured as a sequence of discs equally separated (gray color at the entrance of APIS in Fig. 8).

The detector baffling was obtained by a protrusion of the main part that supported the lens pack (yellow part in Fig. 8). This part was internally milled to fit around the detector chip and to reject incoming lateral light.

2.3.6 *Stray-light analysis*

The APIS camera included a real aperture stop. This stop guaranteed a good performance of APIS with respect to the stray-light rejection factor because it limited the light collected by the CMOS. However, a stray-light analysis of the optomechanical design had to be performed to check the amount of unwanted scattered light reaching the CMOS area.

The simulation was performed with ASAP considering a 1-W emitting Lambertian source covering the whole entrance pupil of the system. The ghost images and the preliminary stray-light behavior of APIS were studied considering the most relevant coatings and paintings of both optical and mechanical parts. Three kinds of coatings with different scattering properties were taken into account in the simulation. The Chemglaze 306 coating was applied to all internal parts of each optomechanical support and to those external parts that would be exposed directly to the optical beam, such as the baffles. The mechanical interface and the rest of the mechanical components were coated with black diffuse, which shows a much higher scattering level for different angles of incidence. The third coating for polished reflective surfaces was applied on some mechanical parts, such as adjustment mechanisms, screws, and the external surfaces of the mechanical structure.

The merit function used to analyze in detail the behavior of the stray-light in the APIS camera was the point source transmittance (PST) curve. The PST associated to the stray-light process was calculated as the ratio of the flux obtained on the focal plane for an incident on-axis collimated beam to the flux collected on the focal plane for an incident collimated beam outside the FOV of the instrument, i.e., from 7 deg to 50 deg (angles outside the maximum semi-FOV of APIS camera).

In the simulation, we separated the flux produced by the beams inside the FOV of the instrument, which produce the image in the CMOS, with respect to the flux produced by the beams scattered in any mechanical surface, which are related to the stray-light process. The results showed that the relative flux received in the image plane due to the scattering in the mechanical surfaces was $\leq 10^{-8}$ times the energy corresponding to the normalized flux directly collected in the CMOS area (inside the FOV). This means that the baffling proposed in the optomechanical design effectively attenuates the unwanted scattered radiation. Figure 9 shows the rejection factor [log (PST)] as a function of the incident angle (only angles out of the FOV are represented).

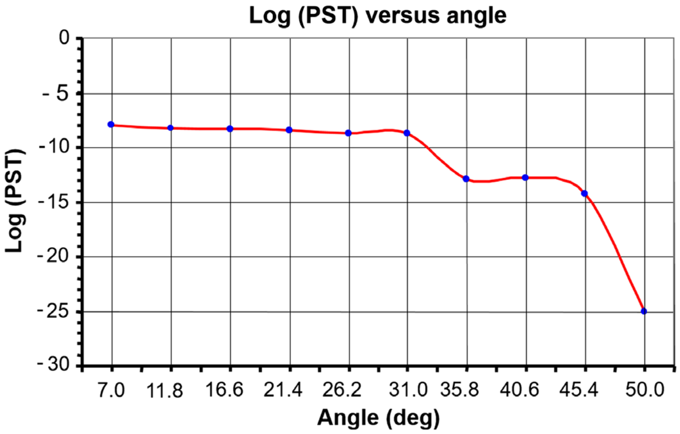

Fig. 9 Logarithm of the irradiance in the focal plane due to the stray-light process.

3 Radiation Test

As it was mentioned in Sec. 1, one of the objectives of the APIS camera was to evaluate the degradation of the commercial glasses and detector during the mission. Therefore, it was necessary to study the behavior of these elements under radiation levels similar to the expected conditions for the OPTOS mission.

The foreseen radiation environment for OPTOS is dominated by the contribution of the Van Allen proton belt. It consists of high-energy protons in the range from 0.01 to >500 MeV. Therefore, a series of ionizing and nonionizing irradiation testing campaigns were performed in order to reproduce the accumulated effects during the mission. The ionizing damage was studied by exposing three optical bread board (BB) models and two BB focal plane boards to a Co^{60} gamma radiation field. In addition, combined ionizing and nonionizing effects were analyzed using a quasimonoenergetic proton source. In this case, another two BB focal plane boards were irradiated with particle fluences equivalent to the estimated mission level.

3.1 *Gamma Radiation Test on APIS Optical BB Models*

The APIS camera included optical glass elements that could be affected by the ionizing radiation. The behavior in radiation environment was already studied for the optical glasses NFK51[15] and NSF57[16] within the LINES research activity for assessing and using COTS glasses in space environment. The behavior for NLASF41 glass was unknown. Therefore, gamma radiation test of this glass and the whole lens set were performed in order to correlate the transmittance loss observed during the mission lifetime.

To estimate the expected transmittance losses during the mission life, three different optical BB models (BB1, BB2, and BB3) were exposed to 5, 10, and 15 krad doses, respectively (corresponding to 1, 2, and 3 mission years). They were made up of optical parallel-plane plates of 8 mm diameter and thickness that closely simulate the elements used in the APIS camera optical design. The doses were calculated according to the mission orbital parameters and the standard models AP8/AE8[17] for the Van Allen belts. The ESP/PSYCHIC[18–20] model for the probability of a solar particle event occurrence was also used. As a conservative approach, AP8/AE8 models were used considering a worst-case scenario of maximum solar activity.

The BB models were exposed to gamma radiation in the Co^{60} pool at the NAYADE facility[21] belonging to the Centro de Investigaciones Energéticas, Medioambientales y Tecnológicas (CIEMAT). The irradiation conditions were 15.7°C temperature, 4.86 krad (Si)/h dose rate, and 9.5% of maximum dose nonuniformity.

The NLASF41 glass showed higher transmission losses than NFK51 and NSF57 glass. The absorption induced by gamma radiation on NLASF41 glass followed the same behavior already observed on NFK51 and NSF57 glass. That means the transmission loss increases as a function of radiation dose following an exponential curve.

Table 1 Transmittance loss data of the optical BB models.

	Wavelength (nm)				
	450	500	560	620	670
Average %T BB models (before irradiation)	56.9	58.4	59.3	59.6	59.7
Δ%*T* BB1 at 5 krad	12.0	10.4	7.3	4.0	2.1
Δ%*T* BB2 at 10 krad	29.6	27.0	21.2	13.8	9.2
Δ%*T* BB3 at 15 krad	38.7	36.3	29.4	19.9	13.7

Transmission measurements versus wavelength of the BB models were carried out before and just after each irradiation test with a Perkin-Elmer Lambda 850 spectrophotometer (±0.08% accuracy).

Table 1 shows the average transmittance data of the three optical BB models before irradiation and the transmittance data difference of each optical BB model before and after irradiation for several wavelengths into the work range.

Therefore, optical transmittance losses (on average) between 7% and 20% (corresponding to one and two mission years) would be enough to observe a performance degradation in the APIS image data and therefore to achieve the scientific goal of the instrument.

3.2 *Gamma Radiation Tests on APIS BB Focal Plane Boards*

Two different BB focal plane boards (M01 and M02) were also exposed to gamma radiation in the Co^{60} NAYADE facility. The irradiation process was performed in six accumulated dose steps: 1, 2.5, 5, 10, 15, and 21 krad, respectively. The irradiation conditions were the same as the ones mentioned in Sec. 3.1.

Electrical characterizations were carried out with the BB focal plane boards before irradiation and after each irradiation step using the IBIS5 evaluation system provided by Cypress Inc. (see Ref. 13). A dark current analysis was performed in order to see the degradation of the active pixels by effect of the radiation. Degradation pixels were considered to have a charge level in dark current >1.91% of the full well charge (62,500 e^-).

The measurements showed an increase on pixel degradation from 10 krad of accumulated dose on both specimens. Figure 10(a) shows the abrupt increment of the pixel degradation by effect of the gamma radiation from 10 krad, and Fig. 10(b) shows the zone between 0 and 5 krad in more detail.

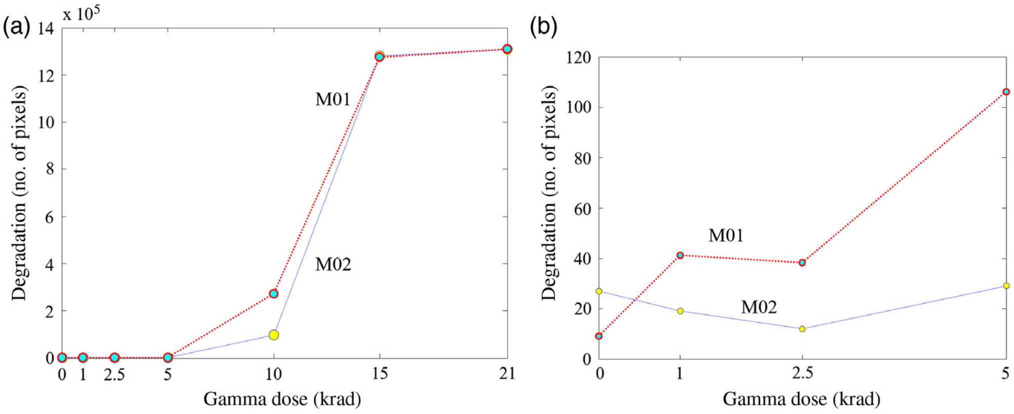

Fig. 10 (a) Pixels with charges in dark current versus gamma radiation dose and (b) detail of the zone from 0 to 5 krad.

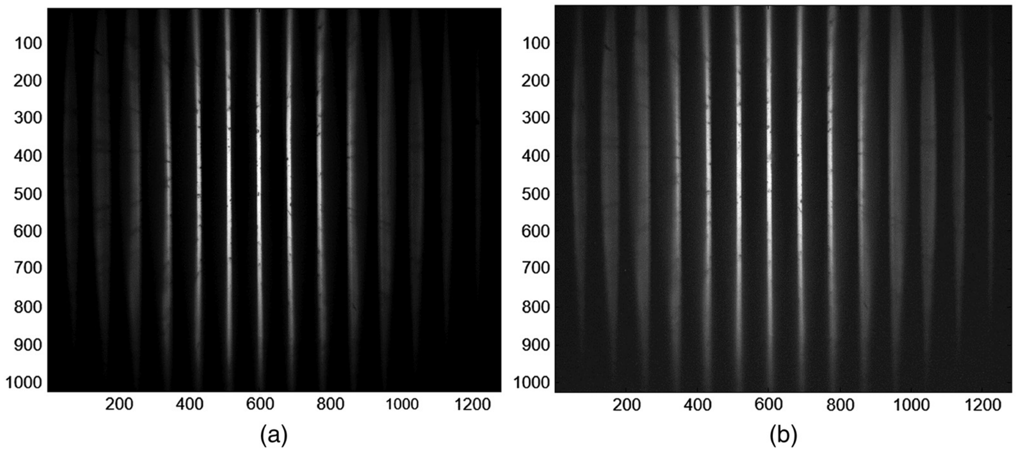

Fig. 11 (a) Foucault test image at 0 krad gamma dose and (b) Foucault test image at 21 krad gamma dose.

Table 2 Image contrast versus gamma radiation dose.

Gamma dose (krad)	Average contrast M01 sample	Average contrast M02 sample
1	0.99	0.99
2.5	0.99	0.99
10	0.92	0.93
15	0.82	0.82
21	0.72	0.65

In addition, an image quality analysis was carried out in order to evaluate the contrast in the images obtained by the CMOS sensor with respect to the gamma irradiation dose. The setup was formed by an LED ($\lambda = 565$ nm), a target (Foucault Test), an optical system, and the CMOS image sensor. Figure 11(a) shows the Foucault test image obtained before the CMOS gamma irradiation, and Fig. 11(b) the Foucault test image after 21 krad of accumulated gamma dose.

The procedure was to calculate the maximum and minimum intensity of the peak patterns obtained for the image central row. The Michelson contrast (visibility) was only estimated using the four central peaks. Table 2 shows the average contrast of the two samples as a function of the gamma radiation dose.

The obtained results guaranteed that changes in the IBIS5-B-1300 sensor could be considered negligible with doses of up to 10 krad of gamma radiation.

3.3 *Proton Radiation Tests on APIS BB Focal Plane Boards*

Another two BB focal plane boards (M03 and M04) were exposed to proton radiation in order to study the effects of the nonionizing radiation damage combined with ionizing effects. These irradiation tests were carried out at the high-energy proton beam line of radiation effects facility, at Jyväskylä University (Finland).[22] In this facility, protons in the energy range from 10 to 50 MeV can be delivered with a homogeneous beam size of 10×10 cm^2. The irradiation process was performed at the maximum available energy of 50 MeV and in six accumulated fluence steps up to a total proton fluence of 1.9×10^{11} cm^{-2} and an equivalent total ionizing dose of ~29.3 krad (see Table 3).

The results showed a similar behavior of the sensor as the one obtained with the gamma irradiation. From the 9.5×10^{10} proton fluence step (14.6-krad ionizing equivalent dose), a

Table 3 50 MeV proton fluence data.

Step	50 MeV proton fluence (p^+/cm^2)	Equivalent accumulated dose [krad (Si)]
1	1.58×10^{10}	2.44
2	3.17×10^{10}	4.88
3	4.75×10^{10}	7.32
4	9.5×10^{10}	14.6
5	1.43×10^{11}	21.9
6	1.9×10^{11}	29.3

Table 4 Number of pixel with charges in dark current versus proton fluence for M04 sample.

50 MeV proton fluence (p^+/cm^2)	Degradation for M04 sample after irradiation (no. of pixels)	Degradation for M04 sample 2 months after irradiation (no. of pixels)
0	131	—
1.58×10^{10}	470	—
3.17×10^{10}	884	—
4.75×10^{10}	1361	—
9.5×10^{10}	8004	—
1.43×10^{11}	141,473	—
1.9×10^{11}	745,335	1,023,394

strong increase of pixels degradation in dark current was observed. Moreover, 2 months after the last irradiation step further increase in pixel degradation was observed. This fact indicated an activation in the time of the samples irradiated with high-energy protons. Table 4 shows the number of pixels with charges in dark current detected in the M04 sample after the irradiation. (The M03 sample data are omitted because of a problem during the irradiation).

On the other hand, the image contrast at the maximum proton fluence (1.9×10^{11}) only showed slight variations as can be seen in Table 5 and Fig. 12.

Therefore, the degradation in the sensor for proton fluences $<10^{11}$ (p^+/cm^2) or <15 krad ionizing equivalent dose can be considered negligible.

Table 5 Image contrast versus proton fluence.

50 MeV proton fluence (p^+/cm^2)	Average contrast M04 sample
1.58×10^{10}	0.98
3.17×10^{10}	0.97
4.75×10^{10}	0.97
9.5×10^{10}	0.95
1.43×10^{11}	0.93
1.9×10^{11}	0.91

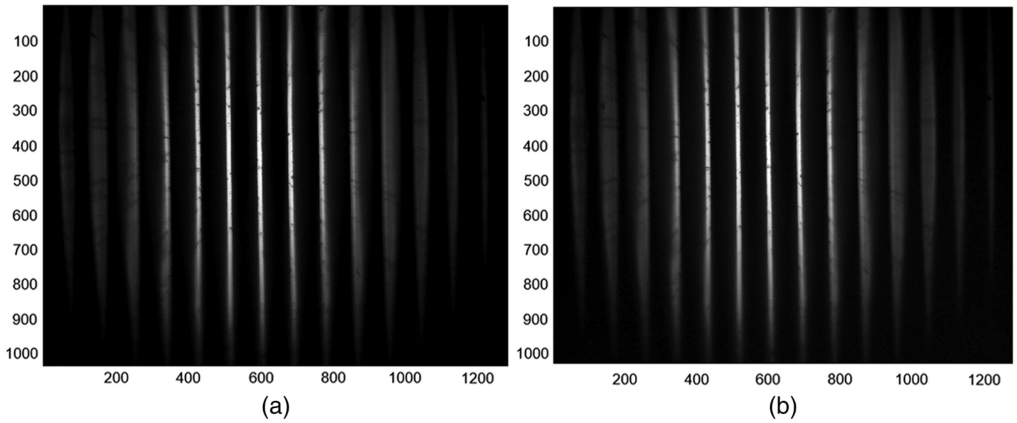

Fig. 12 (a) Foucault test image before proton irradiation and (b) Foucault test image at 1.90 10^{11} proton fluence.

4 Assembly Integration and Verification Phase

The AIV phase of the APIS camera was performed in the LINES ISO-7 cleanroom at INTA. This cleanroom incorporated a 100 class portable clean area and a vacuum chamber, among other ground support equipments.

Three APIS camera units were manufactured: a flight unit and another two units for verification purposes during the AIV phase. This phase was divided in five important steps that are detailed from Secs. 4.1 to 4.5. The MTF of the APIS camera (as the merit function for performance verification) was measured in each of these steps. Previously, a theoretical MTF study had been developed in order to estimate the expected MTF value in each step throughout the AIV phase.

4.1 *Optical Characterization*

The alignment and optical characterization of APIS optical units (without focal plane) were performed with the help of a visible MTF bench from Image Science Ltd. The evaluation of the optical performance was carried out through the measurement of the MTF at the Nyquist frequency (74.6 line pairs/mm) on and off axis. For this AIV phase step, the theoretical MTF had been calculated considering the contribution of three partial MTFs (diffraction, aberration, and alignment/manufacturing tolerances). This theoretical MTF value at the Nyquist frequency was 0.76. A thorough alignment of the lenses for each unit achieved experimental MTF values of 0.76 ± 0.02.

The focal of the three optical units was also calculated from geometrical relationships between the positions of two pinhole images acquired in paraxial approximation. The focal values obtained were within an interval of 20 mm ± 1%.

4.2 *CMOS Sensor Characterization*

The three sensors were characterized in order to set the best configuration parameters for each one. Of particular importance were two parameters: DAC_FINE is used to tune the difference between odd and even columns and DAC_RAW is used to add a general offset (both even and odd columns) to the fixed pattern noise corrected pixel value. These parameters were independently adjusted considering the sensors' behavior in both dark current and flat field simultaneously.

Some other parameters were selected during the characterization as the best default configuration for the sensors. For example, a synchronous (snapshot) shutter to have the light integration on all pixels in parallel; a slow frame/line calibration mode in order to cancel the thermal-KTC noise (reset noise) during the calibration of the output amplifier; a unity gain mode and the internal clock granularities to control the column/pixel readout; and the synchronous shutter sequencer.

4.3 *Electro-Optical Characterization*

The alignment of the APIS focal plane was performed using a 300-mm focal length focusing autocollimator from Trioptics GmbH with ±25-mm focusing range. We established the equivalent relationships between a through-focus, performed around the autocollimator focus, and the corresponding APIS camera focus. To do that, a specific distance between instruments was set.

The theoretical MTF at this step of the AIV phase had been calculated adding the MTFs associated with the detector (footprint, spectral effects, array flatness, and tilt). This theoretical MTF value at Nyquist frequency was 0.46.

The alignment procedure of the APIS focal plane consisted in acquiring a number of images of the autocollimator tilted-cross hair. For each image, the cross hair was placed at different positions around the autocollimator focus. Then, an analysis software, developed in MATLAB, processed these images. The analysis was based on the sloping slit method,[23,24] which allowed finding the best focus position for each APIS camera unit. For each image, the line spread function (LSF_{Data}) of each cross hair arm was obtained and fitted to a Gauss function (LSF_{Gauss}). Figure 13(a) shows the cross hair image of the APIS camera with its labeled arms and Fig. 13(b) shows an example of LSF_{Data} and LSF_{Gauss}.

Then, the full width at half maximum (FWHM) for each LSF_{Gauss} was calculated and these values were fitted to a parabolic function with respect to the autocollimator position [see Fig. 14(a) as an example]. In addition, MTF curves were calculated as the module of the LSF Fourier transform ($|f\{LSF\}|$) for each image: $MTF1 = |f\{LSF_{Data}\}|$ and $MTF2 = |f\{LSF_{Gauss}\}|$. Finally, the MTF values at the Nyquist frequency were fitted to a parabolic curve and plotted as a function of the autocollimator position [see Fig. 14(b) as an example].

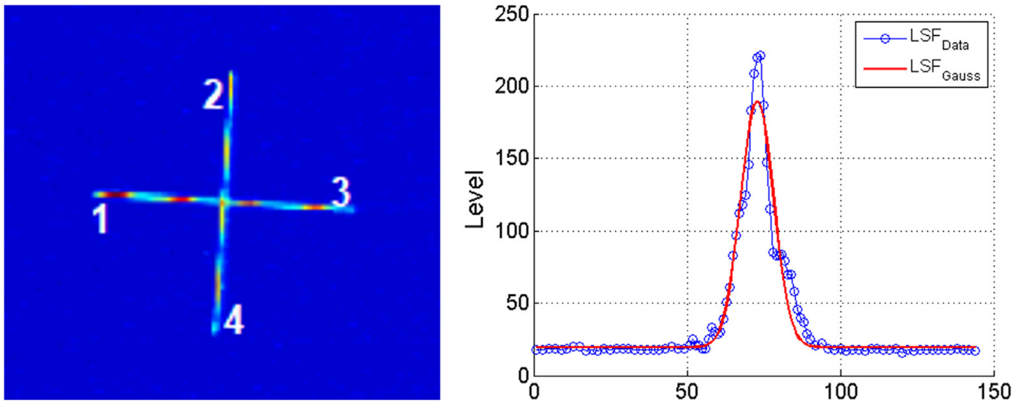

(a) (b)

Fig. 13 (a) Image of the tilted-cross hair and (b) example of LSF_{Data} and LSF_{Gauss}.

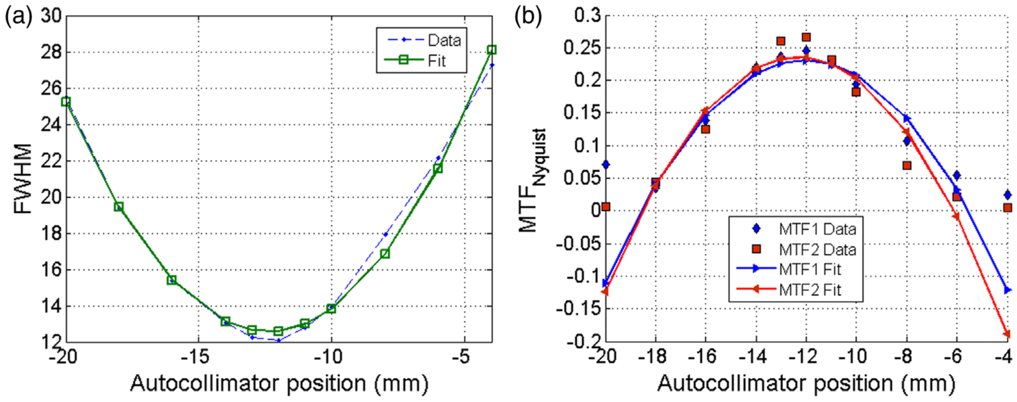

Fig. 14 (a) Example of the LSF FWHM fitting and (b) example of the MTF at Nyquist frequency fitting.

Therefore, the autocollimator position with the minimum FWHM value and the maximum MTF value showed the best focus position of the APIS camera (regarding the equivalent relationships between through-focus).

The alignment procedure of the focal plane for each APIS camera unit achieved MTF values ≥0.40. This experimental electro-optical MTF value at room conditions agreed with a theoretical final MTF in orbit of 0.17 (added MTFs such as atmospheric, jitter, and operational perturbations).

4.4 *Vibration Test*

The object of this test was to validate the APIS electro-optical design and demonstrate the availability of the specimen to withstand the stress, accelerations, and accumulated fatigue damage resulting from the specific vibration environment. For this purpose, one of the APIS camera units was assembled on the OPTOS structural thermal model (STM) that was subjected to its own vibration test. OPTOS STM was vibrated into the Poly-Picosatellite Orbital Deployer (P-POD).

Figure 15(a) shows the OPTOS STM model with APIS camera unit assembled on it and Fig. 15(b) shows the OPTOS STM model (into the P-POD) on top of the vibration platform.

The test was carried out in the Mechanical and Environment Test laboratory at INTA. The following sequence for each axis was applied: low-level sine vibration, high-level sine vibration, low-level sine vibration, high-level random vibration, and low-level sine vibration.

An electro-optical characterization was carried out before and after the test. In addition, dark current and flat field analysis for different integration times were performed before and after the test. The results showed that the vibration environment test did not modify the optoelectronic performance of the APIS payload.

4.5 *Thermal-Vacuum Test*

The object of this test was to check the vacuum induced focus shift, the APIS thermal-vacuum behavior, and the passive athermalization system. The test was carried out in the thermal vacuum chamber (TVC) at LINES ISO-7 cleanroom at INTA. This TVC has optical windows that allowed optical checks during the thermal-vacuum test.

The performed thermal profile, with a warming ramp of 0.2°C/min at 10^{-6} mbar vacuum level, is shown in Fig. 16. The temperatures for image acquisition are marked in the figure with black points. The validation of the passive athermalization system was intended to be performed into the $-20°C$ to $+20°C$ temperature range.

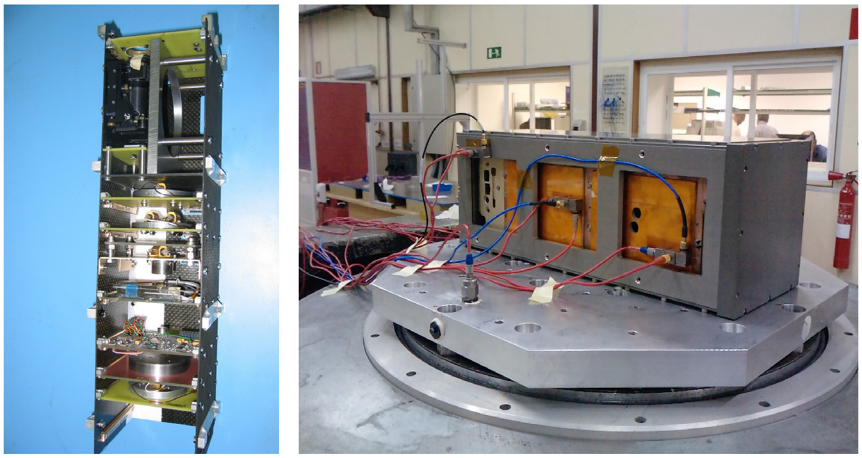

(a) (b)

Fig. 15 (a) APIS unit assembled on the OPTOS STM and (b) OPTOS STM ready on the vibration platform.

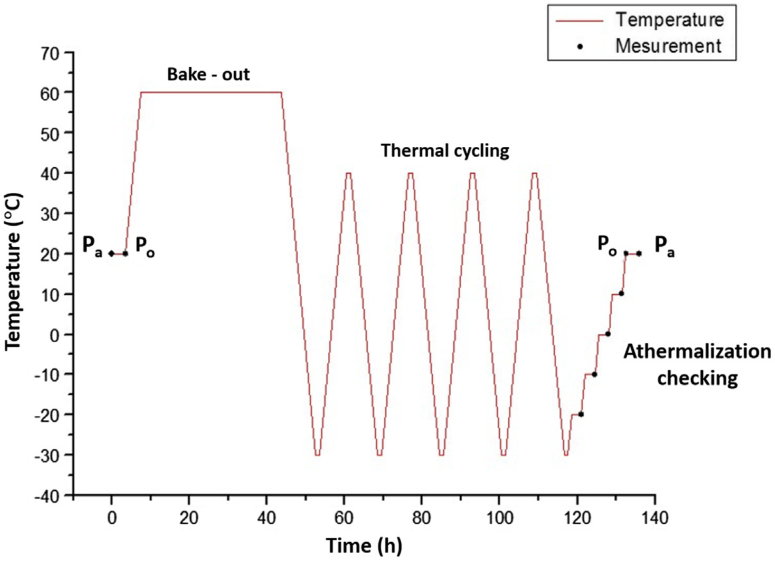

Fig. 16 TVC performed thermal profile.

The APIS camera unit selected for this test was placed inside the TVC, and the focusing autocollimator was outside the TVC and facing the APIS camera through the optical window. Previously, the APIS camera focus at room conditions was shifted -44 μm. This value included the theoretical vacuum focus shift (-26.5 μm) and the thermal focus shift due to changing the temperature from 20°C to 0°C (-17.5 μm) according to CODE V.

An electro-optical characterization was carried out at the black points indicated in Fig. 16 following the procedure/algorithm presented in Sec. 4.3. The equivalent relationships between autocollimator and APIS through-focus were such that 1 mm displacement from the focus of the autocollimator was equivalent to 4.5 μm displacement in APIS focal plane. Therefore, the APIS camera focus depth (± 7 μm) was equivalent to ± 1.6 mm in the autocollimator.

The analysis of the results gave an experimental vacuum focus shift of -22.1 μm, which is according to the theoretical value obtained in Sec. 2.1.1. In addition, the passive athermalization system kept the APIS camera focus inside the focus depth for the complete temperature range. Experimental results can be seen in Table 6.

After the AIV campaign, the APIS camera flight model was assembled in OPTOS CubeSat with the vacuum focus shift applied.

Table 6 Thermal-vacuum test experimental results.

APIS temperature (°C)	Pressure (mbar)	Autocollimator position from focus (mm)	APIS position from focus (μm)	MTF value
+20.85	10^3	−9.8	−44.1	0.42
+19.75	10^{-6}	−4.9	−22.1	0.40
−20.01	10^{-6}	−4.6	−20.7	0.39
−9.77	10^{-6}	−4.1	−18.5	0.40
+0.10	10^{-6}	−3.5	−15.8	0.40
+10.00	10^{-6}	−4.2	−18.9	0.40
+20.50	10^{-6}	−4.1	−18.6	0.39
+20.00	10^3	−8.4	−37.8	0.39

5 APIS Payload Operation

The OPTOS ground segment was formed by an array of four Yagi antennas and a control center located at INTA. The control center performed the spacecraft tracking, the mission control, the commanding, the telemetry processing, the analysis, and the distribution. The APIS image acquisition was always performed via tele-commands sent from the ground. The tele-commands allowed changing the value of some CMOS sensor configuration parameters from the default configuration. The APIS image telemetry included temperature before acquisition, image data, temperature at the acquisition time, result of the acquisition process, and attitude and orbit data.

The operation of the APIS payload was divided into two phases: the first one was carried out with the shutter closed and the second one with the shutter opened. The objective of the first phase was to check the detector and electronics health and the thermal environment of APIS payload during one orbit. In addition, this first phase established the image download time and the image recovery process from the telemetry packages. The procedure during this first phase was to take dark images changing sensor parameters, such as image size (ROI), ROI origin, integration times, etc. The objective of the second phase was to take images of different scenes to study the performance degradation of the images, to perform a georeferencing procedure, and to determine the linear/angular offsets needed for a correct georeferencing.

6 In-Flight Results

OPTOS CubeSat was successfully launched in November 21, 2013. In the summer of 2014, the commissioning phase was ended. During this phase, the Survival On Board Software (OBSW) was validated and the Nominal OBSW was activated and validated in orbit. Therefore, the activation and management of the payloads and the configuration parameters were ready. After that, three payloads of OPTOS were operated in a nominal mode (ODM, FIBOS, and GMR).

The first phase of APIS operation started at the end of January 2015 and lasted until October 2015, alternated with the operation of other payloads. The initial action was to check the thermal environment of APIS payload during one orbit. This point was very important because APIS did not have thermal control. Therefore, this action was carried out several times during the mission lifetime. The orbital points where APIS payload reached the minimum/maximum temperatures were established: $T_{\min} = 24.95°\mathrm{C}$ (5 min after penetrating into the Sun phase) and $T_{\max} = 29.91°\mathrm{C}$ (1 h after penetrating into the Sun phase). The APIS temperatures during the eclipse phase were higher due to the thermal inertia of the instrument but they were not relevant because APIS payload would not be operated during the eclipse. During this first phase, dark images were taken using 8-bit resolution and different ROIs. In that way, the dump time of the images from the sensor memory to the enhanced processing unit by the CAN bus was decreased at a cost of reducing the image size. The ROI origins, integration times, and DAC RAW/DAC FINE parameters were checked. The result was that the detector did not show any performance degradation after almost 2 years in orbit. This fact was in agreement with the results obtained after the radiation test (see Secs. 3.2 and 3.3), since ODM payload reported 0.15 krad per year of accumulated radiation dose ($\sim 10^{-2}$ times the simulated dose during the radiation test).

Unfortunately, the activation of the tasks management related with attitude control failed. At this point, the satellite had been in orbit for more than 2 years. Therefore, the second phase of the APIS operation started at the end of January 2016 without attitude determination and control subsystem (ADCS).

The shutter was opened successfully and the first image was taken on February 5, 2016 over an area of the American state of Wyoming (Medicine Bow National Forest). The parameters of this image were 610 km orbit height, 324×347 pixels (Earth swath of $66\ \mathrm{km} \times 71\ \mathrm{km}$), 204 m resolution, and 2 ms integration time. Figure 17(a) shows the APIS camera first image and Fig. 17(b) the location of the area in Google Earth.

The sensor temperature of APIS, at the time the image was taken, reported a temperature of 47°C due to the reduction of the eclipse phase. The image showed an apparently good focus (note the lower spatial resolution and the presence of clouds and cloud shadows in the APIS image), taking into account the lack of active ADCS, although no quantitative assessment was made.

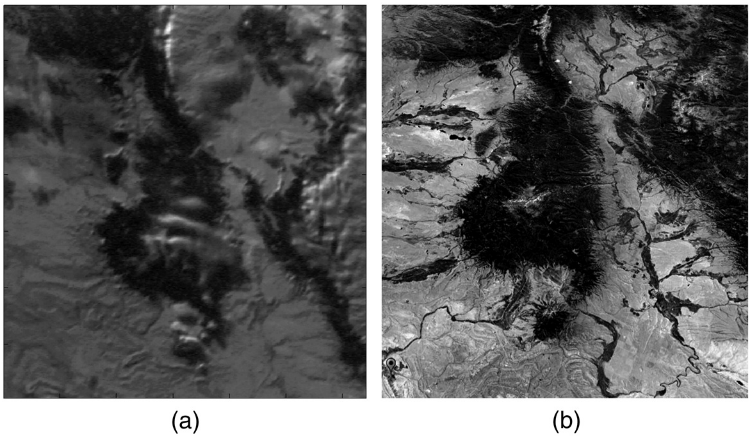

(a) (b)

Fig. 17 (a) APIS camera first image and (b) Google Earth location of the zone.

Even though the acquisition temperature was outside the operating range of APIS, the athermalization system worked satisfactorily.

Taking into account the reported data from the ODM payload, the total ionizing dose measured near the location of the APIS lenses was estimated to be ≤0.4 krad (including conservative margins). The transmission loss of the APIS lenses was theoretically calculated using the software application to predict optical performance loss (due to gamma radiation) developed by LINES laboratory.[16] The value obtained was a 1% transmission loss, which was insufficient to observe optical degradation on glasses through the images (see Sec. 3.1).

The Remote Sensing Group at INTA carried out the image georeferencing procedure. Two images, MOD09GQ.A2016036.h10v04.005.2016038064612.hdf and MOD09GQ.A2016036 .h09v04.005.2016038064855.hdf, taken the same day by the Moderate Resolution Imaging Spectroradiometer (MODIS) instrument of NASA's Terra satellite were used in the process. The two MODIS products were geolocated and mosaicked using simple geolocation software to obtain a single image with similar spatial resolution to the APIS camera. Finally, the APIS camera image was compared with that image.

The MODIS data products were retrieved from the online data pool, courtesy of the NASA Land Processes Distributed Active Archive Center (LP DAAC).[25] Figure 18(a) shows the result of the APIS image georeferencing procedure compared with the MODIS single image [Fig. 18(b)]. This result indicated an OPTOS satellite rotation of almost 50 deg around the Z-axis (nadir). This was an expected OPTOS limitation due to the lack of active ADCS.

After the results obtained from the analysis of this first image, APIS continued taking images of the same size. The integration time was adjusted because the movement of the satellite could produce motion-blur in the images. Figure 19 shows another three APIS camera images: (a) a view of the Ontario area, taken on March 18 at a temperature of 47.3°C; (b) Canadian Artic area, taken on April 1 at a temperature of 35.2°C; and, (c) Canadian Artic area, taken on April 3 at a temperature of 34.4°C, all in 2016.

Figure 20 shows two more APIS images: (a) North of Russia, taken in May 27 (26.8°C), with 483×632 pixels (Earth swath of $104 \text{ km} \times 136 \text{ km}$) and 216 m resolution at 644 km orbit height; and (b) the last image of the APIS camera taken in Northern Canada in September 10 at a temperature of 32°C. The communication with the OPTOS satellite was lost in September 19, 2016 after almost 3 years in orbit.

7 Conclusions

The OPTOS CubeSat could be a suitable platform for simple Earth observation payloads, keeping in mind that its main purpose was technological research. The APIS camera, in turn, has proven to be a robust and valuable instrument. As a result, INTA has already begun the development of a new APIS camera to support an experimental mission based on CubeSat to measure the quality of inland waters. The lessons learned from the OPTOS mission will be used to improve

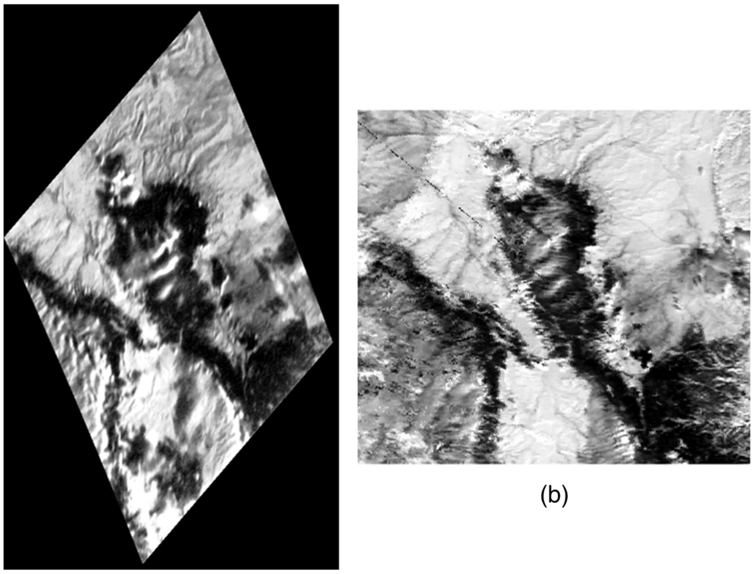
(b)

(a)

Fig. 18 (a) Georeferenced APIS image and (b) MODIS single image.

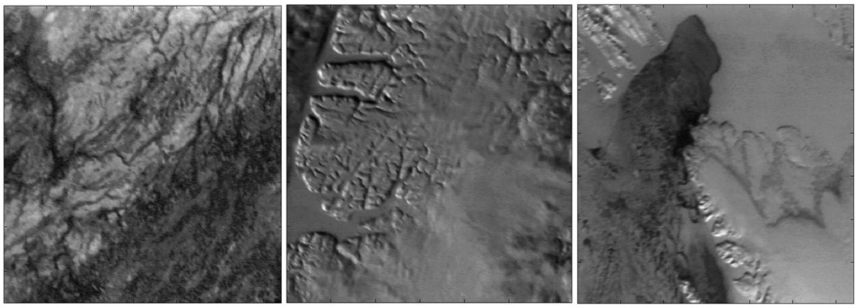
(a) (b) (c)

Fig. 19 (a) Ontario area, (b) Canadian Artic area, and (c) Canadian Artic area.

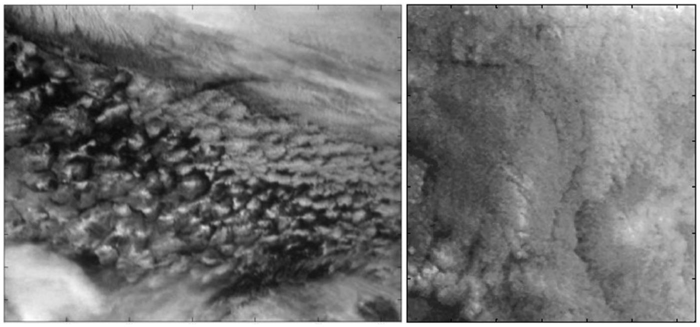
(a) (b)

Fig. 20 (a) North of Russia and (b) the last image of APIS in Northern Canada.

the APIS performance in order to produce useful Earth observation data on such missions and also to pose and test new technological questions.

The use of a passive athermalization mechanical system in cameras with a small #F has been experimentally checked in the laboratory and validated in an LEO, through the APIS images, allowing an operative temperature range greater than 40 K.

The work described in Sec. 3 guaranteed the performance of the IBIS5-B-1300 CMOS sensor on a 2-year Earth observation mission but not for the three commercial glass types used in the APIS camera design. The data obtained in flight about the real accumulated radiation dose (almost 10^2 times smaller), the minimum transmission loss of the APIS camera glass (around 1% theoretically), and the images taken with the APIS camera have demonstrated the viability of using these COTS elements in 2-year Earth observation missions without performance loss.

Acknowledgments

The Centro para el Desarrollo Tecnológico Industrial (CDTI) supported the initial A & B phases of the OPTOS project by financing SENER and THALES Companies. The authors would like to thank Manuel Pérez for the APIS electronic design, Javier Villanueva from Acctiva-Norinstal, S.L. for the APIS mechanical design, and Eduardo Ballesteros and Antonio Liébana from C. A. Asociados, S.L. in charge of the optomechanical manufacturing and assistance with the APIS optomechanical assembly. The authors also thank Concepción G. Alvarado for the specification and design of the bandpass filter and Elisa Muñoz, Amaia Santiago, and César Arza for their assistance during the APIS payload operation phase. Finally, the authors thank Antonio Sánchez, Gonzalo Ramos, Javier Iglesias, Marcos J. Michavila, and Manuel Silva for their support in the development of this instrument.

References

1. A. Mehrparvar, “CubeSat design specification,” in *The CubeSat Program*, CalPoly SLO, San Luis Obispo (2014).
2. I. Lora et al., “INTA picosatellite OPTOS: mission, subsystems, and payload,” in *4th Ann. CubeSat Dev. Workshop*, Huntington Beach (2007). http://mstl.atl.calpoly.edu/~bklofas/Presentations/DevelopersWorkshop2007/Lora_Ivan.pdf.
3. S. Esteve et al., “Small satellite platforms for space environment and effects monitoring,” in *SEENoTC Workshop Data Sharing, Exp. Flight Oppor. and Lessons Learn.*, Toulouse (2008).
4. C. Cazorla et al., “Attitude determination and control strategies for the OPTOS picosatellite,” in *ISU Alumni Conf.*, Barcelona (2008).
5. INTA, “Optical wireless for intra-spacecraft communications,” in *CCSDS Fall Meeting–Wirel. Working Group*, Berlin (2008). https://cwe.ccsds.org/sois/docs/SOIS-WIR/AAA%20Meeting%20Materials/2008/Fall/CCSDS%20-%20BERLIN%202008%20-%20Optical%20Wireless%20for%20intra%20Spacecraft%20Communications.pdf.
6. J. M. Encinas, “OPTOS STM - results and satellite validation,” in *6th Ann. CubeSat Dev. Workshop*, San Luis Obispo (2009). http://mstl.atl.calpoly.edu/~bklofas/Presentations/DevelopersWorkshop2009/5_Encinas-OPTOS.pdf.
7. P. Cabo et al., “OPTOS: a pocket-size giant (mission, operation, and evolution),” in *Proc. AIAA/USU Conf. Small Satell., The Smaller Elements, SSC09-X-11*, Logan (2009). https://digitalcommons.usu.edu/smallsat/2009/all2009/67/.
8. G. Albaladejo et al., “Highly efficient CubeSat platform: project OPTOS,” in *59th Int. Astronaut. Congr. (IAC)*, Glasgow, IAF Ed. Proc. IAC, Vol. **7**, 08.B4.6.A3, pp. 4183–4191 (2008).https://iafastro.directory/iac/archive/browse/IAC-08/B4/6.A/2081/.
9. C. Martínez et al., “OPTOS project: new generation of innovative satellites,” in *4S Symp. Small Satell. Syst. Serv.*, Funchal (2010).
10. C. Arza et al., “OPTOS: STM result, satellite validation and future evolution,” in *60th Int. Astronaut. Congr.*, Daejeon, IAF Ed. Proc. IAC, Vol. **5**, IAC-09.B4.1.8, pp. 3460–3470 (2009). https://iafastro.directory/iac/archive/browse/IAC-09/B4/1/5391/.
11. V. M. Aragón et al., “Researching a robust communication link for CubeSat: OPTOS, a new approach,” in *SPACOMM 2011: Third Int. Conf. Adv. in Satell. and Space Commun.*, Budapest, pp. 45–50 (2011). http://www.thinkmind.org/download.php?articleid=spacomm_2011_3_20_30059.

12. C. Martinez, "OPTOS," in *5th CubeSat Dev. Workshop*, San Luis Obispo (2008). http://mstl.atl.calpoly.edu/~bklofas/Presentations/DevelopersWorkshop2008/2-OPTOS-Cesar_Martinez.pdf.
13. Cypress Semiconductor Corporation, Document #: 38-05710 Rev. *A, San Jose (2007).
14. M. Silva-López et al., "Analysis and evaluation of the Full Disk Telescope refocusing mechanism for the Solar Orbiter mission," *Opt. Eng.* **54**(8), 84104 (2015).
15. M. Fernández-Rodríguez et al., "Modeling of absorption induced by space radiation on glass: a two-variable function depending on radiation dose and post-irradiation time," *IEEE Trans. Nucl. Sci.* **53**(4), 2367–2375 (2006).
16. M. Fernández-Rodríguez, *De los efectos del ambiente espacial en las propiedades ópticas de vidrios y recubrimientos para sistemas espaciales*, Chapters 4 and 7, INTA Ministerio de Defensa, Madrid (2017).
17. J. I. Vette, "Trapped radiation environment model program (1964–1991)," in *NASA/Natl. Space Sci. Data Center, NSSDC/WDC-A-R&S 91–29*, Greenbelt (1991). https://ntrs.nasa.gov/archive/nasa/casi.ntrs.nasa.gov/19930001815.pdf
18. M. A Xapsos et al., "Probability model for worst case solar proton event fluencies," *IEEE Trans. Nucl. Sci.* **46**, 1481–1485 (1999).
19. M. A Xapsos et al., "Probability model for cumulative solar proton event fluencies," *IEEE Trans. Nucl. Sci.* **47**, 486–490 (2000).
20. M. A. Xapsos et al., "Model for cumulative solar heavy ion energy and linear energy transfer spectra," *IEEE Trans. Nucl. Sci.* **54**(6), 1985–1989 (2007).
21. Centro de Investigaciones Energéticas, Medioambientales y Tecnológicas (CIEMAT), http://www.ciemat.es/sweb/SEPA/Instalaciones/Html/Pdf/93.pdf.
22. A. Virtanen, "Radiation effects facility RADEF," in *Proc. Eighth IEEE Int. On-Line Test. Workshop (IOLTW 2002)*, Isle of Bendor, p. 188 (2002).
23. T. L. Williams, *The Optical Transfer Function of Imaging Systems*, Chapter 10, Institute of Physics Publishing, London (1999).
24. G. D. Boreman, *Modulation Transfer Function in Optical and Electro-Optical Systems*, SPIE Press, Bellingham (2001).
25. National Aeronautics and Space Administration (NASA), "Land processes distributed active archive center," https://lpdaac.usgs.gov/data_access/data_pool.

Daniel Garranzo received his BS degree in physics in 2002, with a specialization in physical and control devices, and his MS degree in 2006 from the Complutense University of Madrid (UCM). In 2004, he joined the Spanish National Institute for Aerospace Technology (INTA) as an optical engineer. His experience includes optical metrology, alignment, verification and integration of space optical instrumentation, and qualification of devices and materials for space applications.

Armonía Núñez received her BS degree in physics (optics) from the University of Zaragoza in 1989. Since 1994, she has been working as an optical engineer in the area of space optics at the National Institute of Aerospace Technology (INTA). Her experience includes optical design, integration, and verification of space optical instrumentation, and characterization and modeling of optical materials exposed to space environments.

Hugo Laguna received his senior technician in electronic product development degree at the IES Madrid in 1998 and graduated in optics and optometry at the UCM-Faculty of Optics in 2012. Since 1998, he has been working as an electro-optical engineer at the INTA, first in the Department of Aeronautical Programs, and from 2008 to the present in the area of space optics.

Tomás Belenguer has been a member of the INTA technical staff since 1995. He has developed a career in optical engineering applied to industrial and space optical systems and equipment. He has more than 20 years of experience in design, integration, and characterization of optical instrumentation and more than 15 years of experience in space programs. Since 1986, he has belonged to the Laboratorio de Instrumentación Espacial and he is currently the head of the Spatial Optics Area at INTA.

Eduardo de Miguel is the head of the Remote Sensing Systems Group at the INTA. He has been working since 1992 in spaceborne and airborne remote sensing projects. Most of his work has been related to specification, implementation, and validation of processing and archiving facilities, including HW/SW issues, processing algorithms, and user services. He has also participated in the definition of space and ground segment requirements for a number of Earth observation missions.

María Cebollero received her BS degree in physical sciences in 2005 from the Autonomous University of Madrid (UAM) in the specialty of applied sciences. Since 2006, she has been working at the INTA in space systems engineering, developing tasks as satellite operator, thermal engineer, and AIV responsible person.

Sergio Ibarmia received his BS and MS degrees in atomic, nuclear, and molecular physics in 2003 from the UCM. In 2005, he joined to the INTA as a radiation engineer in the Space Programs Department. His work at INTA has included radiation-shielding design for space missions, radiation hardness assurance and component testing, and development of high-energy particles simulation techniques.

César Martínez has been the head of the Small Satellites Program at INTA since 2009. He earned his BSc degree in aerospace engineering from Polytechnic University of Madrid in 1993, his MSc degree in physics from Open University in 1998, and his PhD in telecommunications from the University of Vigo in 2016. He has wide experience in management and engineering of space programs.